



# Numerical and experimental benchmark solutions on vibration and sound radiation of an Acoustic Black Hole plate

Li Ma, Li Cheng\*

Department of Mechanical Engineering, The Hong Kong Polytechnic University, Hong Kong

## ARTICLE INFO

### Article history:

Received 31 October 2019

Received in revised form 11 January 2020

Accepted 15 January 2020

### Keywords:

Acoustic Black Hole (ABH)

Daubechies wavelet (DW) model

Benchmark solutions

Vibration and noise control

## ABSTRACT

Acoustic Black Hole (ABH) has been attracting the ever-increasing attention from the scientific community as a passive, effective and lightweight solution for vibration and noise mitigations of vibrating structures. Most existing work, however, relies on numerical simulations using Finite Element models, except a few cases where alternative methods are attempted. In general, there is a lack of well-calibrated experimental benchmark solutions for model validations and phenomena assertions, especially in 2D cases where precise fabrication of ABH indentations with well-controlled thickness profile is a challenge. In this paper, a rectangular plate embodied with a symmetric circular ABH indentation is meticulously manufactured and experimentally tested in terms of eigen-frequencies, mode shapes, forced vibration response and radiated sound power in a baffled half-space. These results offer useful benchmark solutions for future ABH studies. In particular, experimental results show a high consistency with the ones predicted by the previously developed 2D Daubechies wavelet (DW) model.

© 2020 Elsevier Ltd. All rights reserved.

## 1. Introduction

The mitigation of structural vibration and its noise radiation has been a long-lasting issue, relevant to many applications. Vibration reductions via viscoelastic coating over the structural surface [1] or reducing wave reflections from structural boundaries such as graded impedance interface [2] are among a few popular options for achieving highly damped structures. However, the need for lightweight structures poses new challenges to these conventional solutions. As an alternative, structural design based on Acoustic Black Holes (ABHs) phenomena [3,4] shows promise for controlling flexural vibrations in thin-walled structures alongside a possible weight reduction. Taking advantage of smoothly decreasing structural thickness, tailored according to a power-law relationship, an ABH structure exhibits progressively reduced flexural wave phase velocity towards the tapered/indentation area, giving rise to pronounced energy focalization and reduced wave reflections with the use of a small amount of damping material [4,5]. As a promising passive and lightweight solution, interests in exploring ABH effects for various vibration and noise control have been experiencing an exponential growth during the past decade [5–15].

As analytical solutions on realistic ABH structures are practically unavailable, most existing work resorts to numerical simulations using Finite Element method [10,11,16,17] or other

alternative techniques [18,19]. In relation to these works, comparisons with experimental results, in views of model validations, are scarce in the literature. Among a few existing examples, one can cite O'Boy et al. [18] who investigated the damping and the mobility of a rectangular plate containing a wedge of power-law profile using a bending plate model. However, positions of resonant peaks showed significant differences with the results obtained from experiments. Experimental investigations into vibration characteristics of ABH plates have also been carried out in Refs. [7,11,19]. As opposed to vibration analyses [20–23], explorations into sound radiation properties of ABH structures are scarce. Bowyer and Krylov [9] firstly experimentally investigated the sound radiation properties of rectangular plates containing multiple circular indentations. While demonstrating some typical ABH phenomena and their vibration and acoustic benefits, it is observed that the experimental setup may cause some errors at low frequencies because of the acoustic short circuiting resulting from the free edges of the plate due to the absence of the acoustic baffle.

Simulation models are of vital importance for carrying out ABH design, analyses and optimization. However, there is still a lack of well-calibrated experimental benchmark solutions for their validations. This is probably due to the challenging task of manufacturing high-precision ABH indentations. In fact, as demonstrated by Bowyer et al. [24], ABH effects show strong dependence on geometrical details. Although effective damping of ABH structures can still be obtained with the existence of imperfect geometrical and material parameters, such a variability can be a serious issue from the

\* Corresponding author.

E-mail address: [li.cheng@polyu.edu.hk](mailto:li.cheng@polyu.edu.hk) (L. Cheng).

viewpoint of model validations. Therefore, it is imperative to establish a full set of well-controlled benchmark solutions, which motivates the present work.

In this paper, a rectangular plate embedded with a symmetric circular ABH indentation was meticulously manufactured using Computer Numerical Control (CNC) milling. Structural properties of the manufactured sample, such as eigen-frequencies, mode shapes, forced vibration response and sound radiation into a baffled half-space were then experimentally measured and compared with the predictions by a previously developed Daubechies wavelet (DW) model. The objective of the paper is twofold: offering a useful set of experimental benchmark solutions for future ABH studies; and validating the previously developed model along with the experimental assertion of the revealed ABH-specific phenomena.

The rest of the paper is structured as follows. Section 2 briefly revisits the previously developed DW model. Section 3 gives a description of the high-precision ABH manufacturing process. In Section 4, experimental setup used for vibration and sound radiation tests are introduced, followed by a brief description of the sound power measurement procedure. Comparisons between the experimental results and DW model predictions are then conducted in Section 5, in terms of eigen-frequencies of the first 120 modes, mode shapes, forced vibration response and radiated sound power. Finally, conclusions are summarized in Section 6.

## 2. System description and benchmark semi-analytical model

For the completeness of the paper, this section gives a brief account of a previously developed 2D ABH plate model [13] surrounded by an infinite rigid baffle. As shown in Fig. 1, the plate (with a lateral dimension of  $a, b$ ) incorporates a symmetric circular ABH indentation whose thickness is tailored according to  $h(x, y) = \varepsilon r^\gamma + h_0$ , where  $\varepsilon$  is a constant,  $\gamma$  the power law index,  $r$  the distance from the observing point to the ABH center ( $x_c, y_c$ ),  $h_0$  represents the minimum thickness of the indentation. The radius of the circular indentation is denoted by  $R_{ABH}$ . The region outside the ABH indentation of the plate has a uniform thickness  $h$ . The plate is supported by a set of artificial springs, both translational and rotational, that are uniformly distributed along the edges. The ABH indentation is partially coated with damping layers on both sides. The damping of the system is included using complex Young's modulus that incorporates the loss factor of material:  $E_0^* = E_0(1 + i\eta_0)$  and  $E_d^* = E_d(1 + i\eta_d)$  represent complex Young's moduli of the plate and the add-on damping layers, respectively;  $\eta_0$  and  $\eta_d$  are the corresponding loss factors. The damping layers are integrated with the plate and are considered in a fully coupled manner in the model. The plate is subject to a harmonic mechanical point force  $f(t)$  at the uniform portion of the plate.

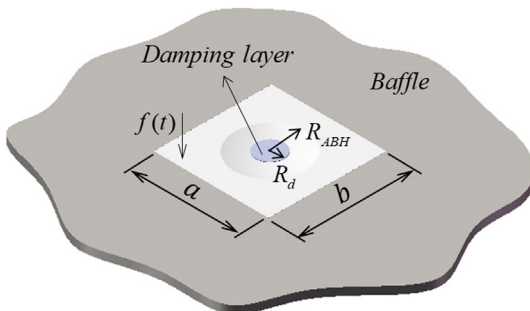


Fig. 1. Modelling of the ABH plate.

The solution to the established model is based on the Kirchhoff-Love thin plate theory under the framework of the Rayleigh-Ritz method, after decomposing the plate transverse displacement  $w$  as

$$w = \sum_{i=1}^p \sum_{j=1}^q a_{ij}(t) \varphi_i(\xi) \varphi_j(\eta) \quad (1)$$

where  $\xi = x/a$  and  $\eta = y/b$  are the dimensionless coordinates,  $\varphi_i(\xi)$  and  $\varphi_j(\eta)$  are the Daubechies wavelet (DW) admissible functions. The discretized matrix form of the equation of motion of the system writes [25]:

$$(\mathbf{K} - \omega^2 \mathbf{M}) \mathbf{A} = \mathbf{F} \quad (2)$$

where vector  $\mathbf{A}$  contains the amplitudes of complex coefficients  $a_{ij}(t)$ ;  $\mathbf{M}$  and  $\mathbf{K}$  respectively stand for the global mass and stiffness matrices;  $\omega$  is the circular frequency;  $\mathbf{F}$  is the vector of the excitation force. Eq. allows obtaining the eigen-frequencies and corresponding mode shapes upon solving its eigenvalue problem or the forced vibration response. Subsequently, the sound power radiated into a baffled half-space can be obtained as [25]:

$$W_{rad} = \mathbf{V}^H \mathbf{R} \mathbf{V} \quad (3)$$

where  $\mathbf{V}$  is the vector of vibration velocity,  $\mathbf{R}$  the radiation resistance, and the superscript  $H$  the complex conjugate. Results predicted by the DW model will be verified by experimental tests on a manufactured test sample.

## 3. Manufacturing process of ABH test sample

The manufacturing procedure of an ABH plate sample and the parameters that control the manufacturing process are reported as follows. To quantify the deviation of the manufactured thickness profile from its pre-designed one, the thickness at multiple points over the manufactured profile is measured using a Coordinate Measuring Machine (CMM).

The designed geometrical parameters of the test sample are shown in Table 1. Material parameters of ABH sample and those of the damping layer (3M™ VHB™ adhesive transfer tape F9473PC) are tabulated in Table 2. The damping material used in the tests is produced by 3M Company.

### 3.1. Manufacturing method

Manufacturing metallic structures with a thin thickness is technically challenging, especially for an ABH plate that incorporates an indentation with a power-lawed profile variation. The minimum thickness that can be reached in commonly used manufacturing techniques such as CNC milling and 3D printing is around 0.5 mm. In the present case, the targeted minimum thickness at the center of the indentation is chosen to be 0.6 mm. Meanwhile, the radius of the ABH indentation is relatively large, i.e., 0.15 m. All in all, two main concerns arise. First, suffering from the mechanical stress from the milling cutter, the thin area of the ABH indentation is susceptible to tearing. Second, the resulting high-temperature stress may deform the thin indentation area, thus compromising the accuracy of the thickness profile. Therefore, materials of the test sample and the milling cutter should be carefully selected. In the present case, top-grade aluminum 7075 which is widely used in aerospace industry is chosen. Aluminum 7075 has good machinability with high strength resistance to mechanical

Table 1  
Geometrical parameters.

$a = 0.6$ m	$x_c = 0.3$ m	$\varepsilon = 0.24/\text{m}$
$b = 0.5$ m	$y_c = 0.25$ m	$\gamma = 2$
$h = 6$ mm	$h_0 = 0.6$ mm	$R_{ABH} = 0.15$ m

**Table 2**  
Material parameters.

	Density	Elastic modulus	Loss factor	Poisson's ratio
ABH plate	$\rho_0 = 2800 \text{ kg/m}^3$	$E_0 = 71 \text{ GPa}$	$\eta_0 = 0.002$	$\mu_0 = 0.33$
F9473PC	$\rho_d = 980 \text{ kg/m}^3$	$E_d = 30 \text{ MPa}$	$\eta_d = 0.9$	$\mu_d = 0.499$

stress. Also, the sufficiently tough tungsten cutter with a ball end is a preferable choice for milling. The parameters that determine the manufacturing process should also be meticulously controlled. The rotation speed of the cutter is expected to be high, up to 10,000 rpm. Also, the cutting volume and the cutting step of the milling cutter should be small, which are 0.5 mm and 0.15 mm, respectively.

The manufacturing procedure mainly consists of four steps. Firstly, a flat plate which has the same size as the test sample was machined out from an aluminum block with the burs being removed, while the flatness error of the surface on both sides is controlled within an acceptable level, e.g. 0.05 mm for the present case. Secondly, the milling cutter produced the ABH indentation following a circular path around the center of the indentation, from outside toward inside. Meanwhile, cooling liquid was used to alleviate the induced high-temperature stress. Finally, after completing the indentation on the top side of the plate, the sample was set aside for stress release for several days. Prior to manufacturing the symmetric indentation on the other bottom side, the finished indentation on the top side was fully filled with a plaster to alleviate possible flapping of the cutter. Note the flapping effect frequently occurs when machining thin metals during CNC milling, which can even lead to the tearing of the structure if not properly refrained. Meanwhile, sufficient machining allowance should be considered in each manufacturing step. Following the procedure described above, the symmetric indentation was successfully produced using a three-axis CNC milling machine (type VSC-1470).

### 3.2. Accuracy of the manufactured ABH profile

The manufactured test sample contains inevitable geometrical imperfections because of machining precision. Therefore, the deviation of the manufactured indentation from its predesigned profile is checked through measurement.

For illustration purposes, the half thickness, defined as the distance from a point at the surface of the indentation to the mid-plane of the test sample, is used to evaluate the error of the manufactured profile. On the top side, 31 measurement points (including the ABH center point) uniformly distribute along two perpendicular lines intersecting at the ABH center, as shown in Fig. 2(a). The thickness profile variations along these two perpendicular lines, for a total of four profile trails (numbered 1<sup>#</sup>, 2<sup>#</sup>, 3<sup>#</sup>, and 4<sup>#</sup>), were examined and deviations of them from the predesigned profile were assessed. The projection of these profiles and the points onto the mid-plane is shown in Fig. 2(a). The half thickness profile of these 31 points was measured using CMM. Similar measurement was also carried out for the bottom side of the plate. The half thickness variations obtained for both sides are respectively shown in Fig. 2(b) and (c), in comparison with that of the predesigned standard profile.

As can be seen from Fig. 2(b), for the top side, the half thickness for points over the four measured profile trails are very similar. This similarity can also be observed for the bottom side. Furthermore, the half thicknesses at four points located at the same circle are averaged, both for the top side and bottom side, and compared with their predesigned counterpart in Fig. 2(d). It can be seen that, the half thickness on the top side shows a nice agreement with that of the predesigned profile, while a marginal deviation is observed

for the bottom side, particularly at the central part (within a radius of 50 mm) of the indentation. However, this slight deviation is deemed to be acceptable, as will be further demonstrated by the agreement of vibration response between experimental tests and numerical simulations in Section 5.

## 4. Experimental setup

The vibrational properties of the manufactured sample and its radiated sound field were measured, inside a test room and a fully anechoic room, respectively. This section reports the experimental setup used for both tests.

### 4.1. Measurement of vibration characteristics

The test sample was vertically suspended onto a rigid frame using two flexible strings that introduce negligible damping, allowing for the vibration testing of the sample under free boundary conditions. The two strings pass through small holes (with a diameter of 4 mm) near the corner of the sample, as shown in Fig. 3(a). The strings maintain adequate strength to support the weight of the sample plate (about 4.8 kg). The plate was excited by electromagnetic shaker (type 4809) through a small thin rod/stinger to filter out possible moment excitation. A force transducer (B&K 8200) was installed to the end of the stinger to measure the input force. To reduce possible mass loading effect, adhesive glue was used to connect the force transducer to the test sample, as shown in Fig. 3(b). The electromagnetic shaker was fed by a power amplifier (B&K 2706) with the periodic chirp signal. The input signal was converted to voltage signal via a charge amplifier (B&K 2635). A Polytec scanning laser vibrometer (PSV) 400 was used for signal generation and data acquisition. The vibration response signals were averaged over ten measurements to guarantee statistically representative results.

### 4.2. Measurement of the radiated sound power

The measurement of the radiated sound power was carried out in a fully anechoic chamber with an inner dimension of  $6 \times 6 \times 3$  m. The cut-off frequency of the chamber is roughly 90 Hz. A B&K Pulse system was utilized for signal generation and data acquisition instead of PSV 400, while other equipment remaining the same as for the vibration test. Thick large wooden panels (8 long  $\times$  8 ft wide  $\times$  0.75 inch thick) were used to surround the test sample to form a rigid acoustic baffle. Four smaller wooden panels, 4 ft long  $\times$  4 ft wide  $\times$  0.75 inch thick, were annexed to the four edges of the baffle to constitute a folded wall (see Fig. 4(a)), which allows for a larger effective sound wave blockage area. The test plate, flush-mounted with the surface of the baffle, was installed in the middle of the baffle, as shown in Fig. 4(b). The gap between the wooden panel and the test sample was around 1 mm to avoid additional damping to the test sample caused by friction. The electromagnetic shaker was sealed inside a thick-walled box made of Polymethyl methacrylate to minimize its direct sound generation. The linearity of the system was ensured by checking the sound power outputs while doubling the input force level. The schematic of the experimental setup is shown in Fig. 5.

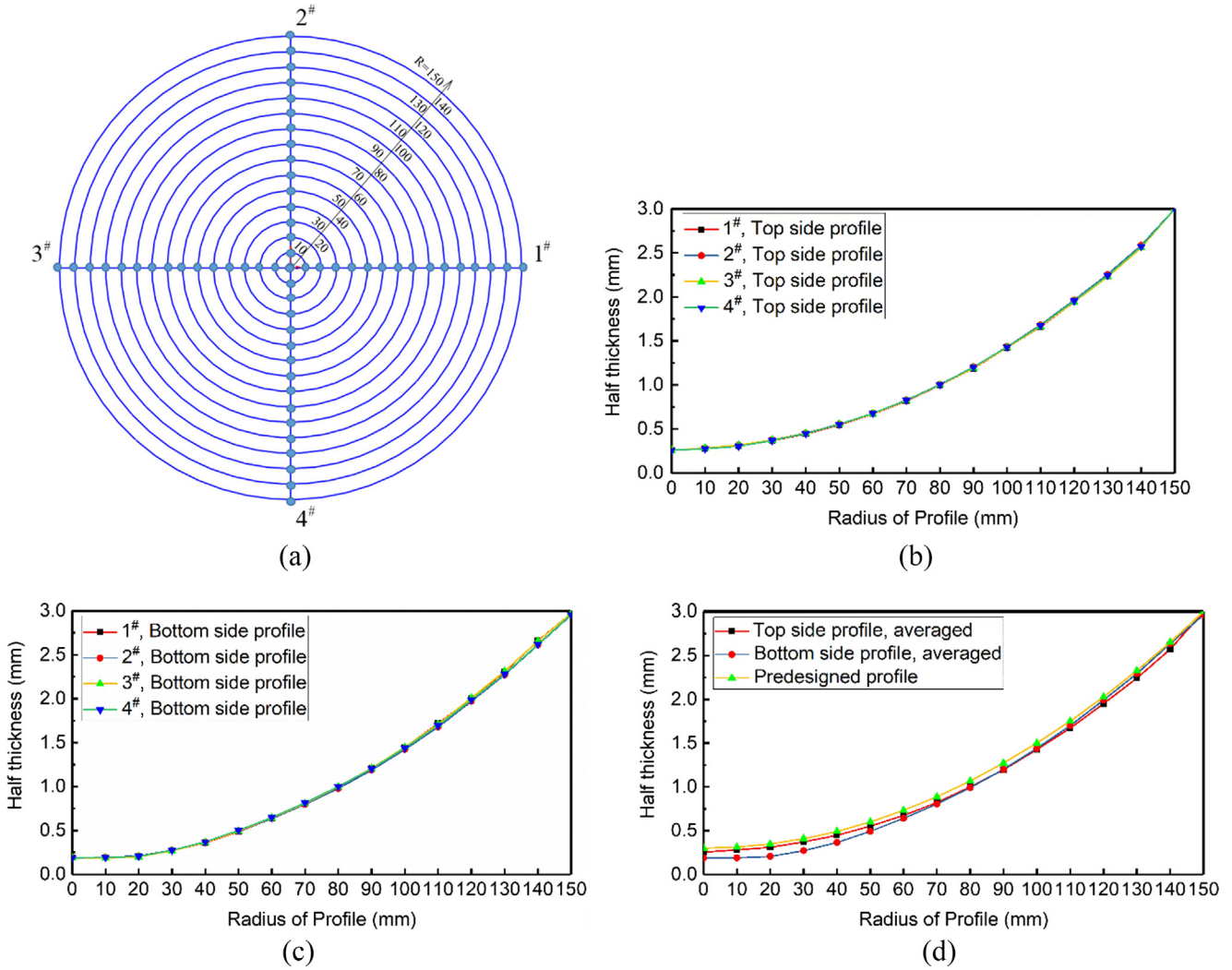


Fig. 2. Half thickness profile: (a) measuring points; (b) top side; (c) bottom side; (d) averaged manufactured profile and predesigned profile.

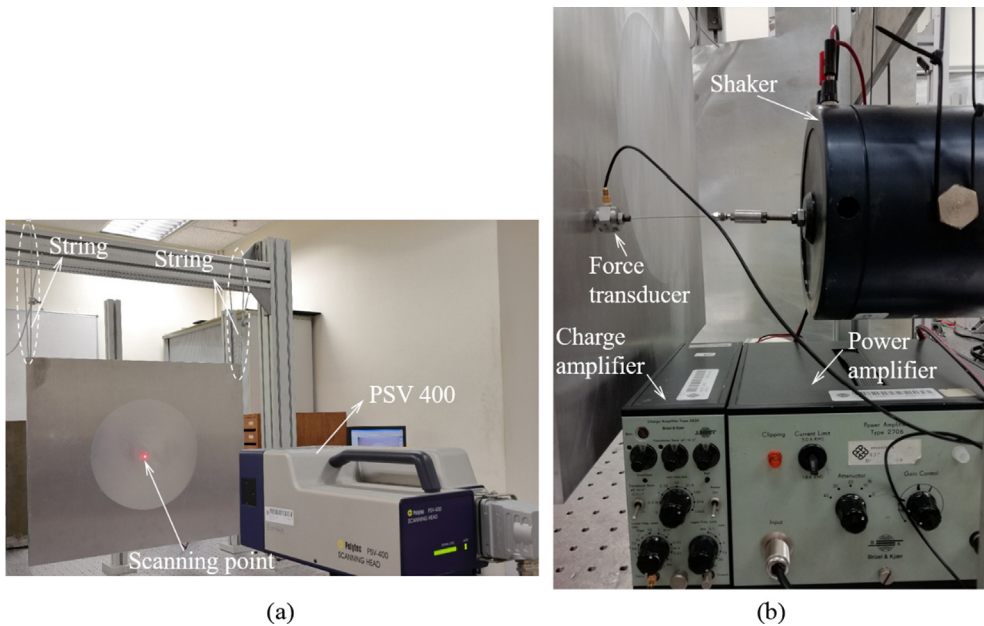


Fig. 3. Experimental setup: (a) ABH test sample; (b) excitation with electromagnetic shaker and force transducer.

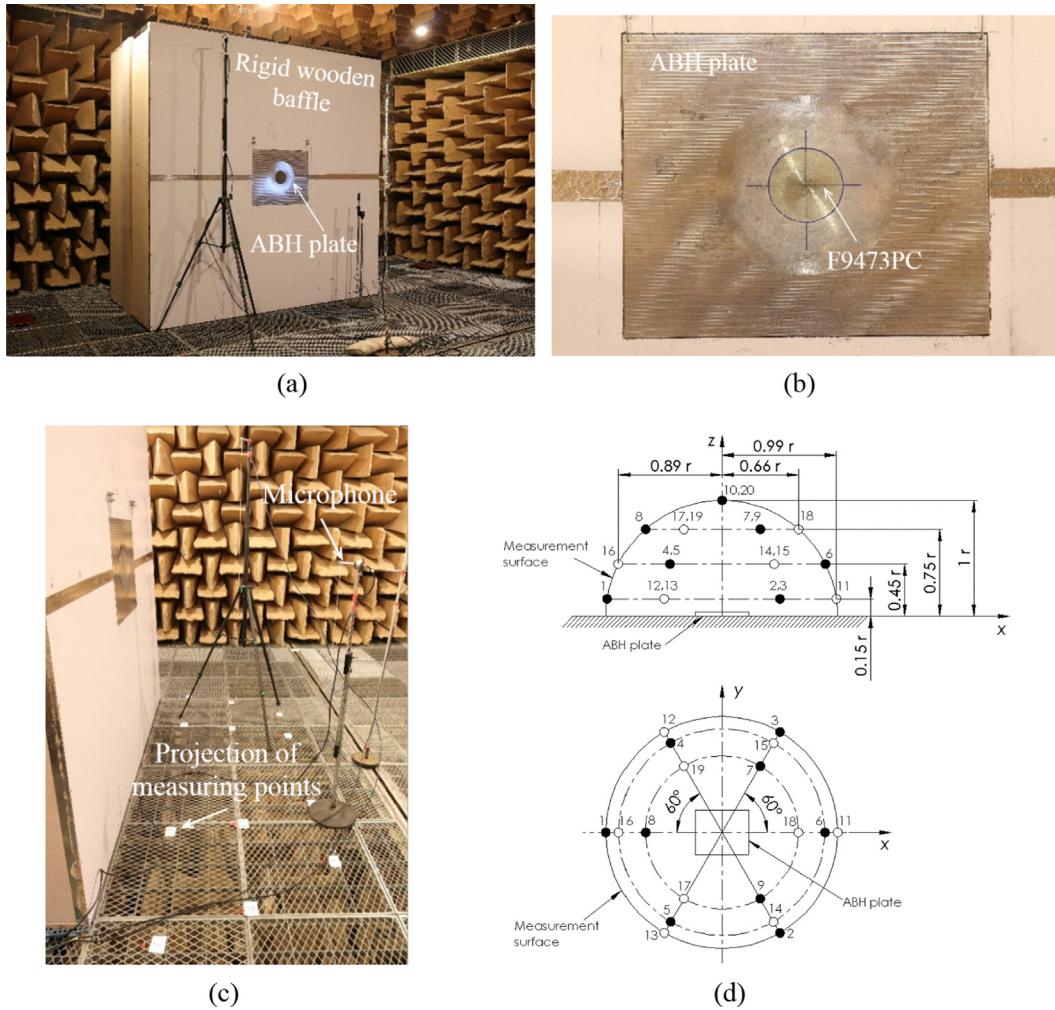


Fig. 4. Anechoic chamber for radiated sound power tests: (a) position of the ABH test sample in relation to the rigid baffle; (b) coverage of the viscoelastic material F9473PC; (c) measuring points projected on the floor (red dot); (d) microphone positions over the hemispherical surface.

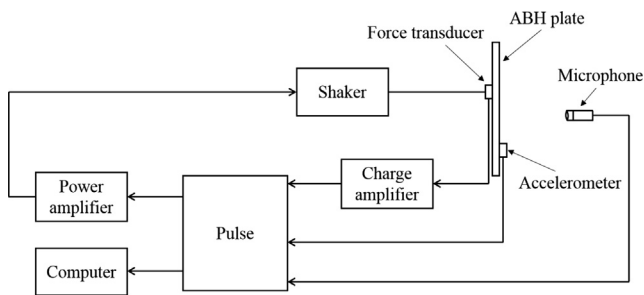


Fig. 5. Schematic of the sound radiation test.

The sound power was obtained through sound pressure measurement in accordance with the international standard ISO 3744 [25]. Twenty microphones were installed over an assumed hemispherical surface enclosing the front panel, as shown in Fig. 4(d), with their projection on the floor of the chamber shown in Fig. 4 (c). The radius of the hemispherical surface should be larger than twice the characteristic source dimension of the test sample (1.78 m for the current case). In the current case, microphones were positioned on a hemispherical surface with a radius of 1.3 m due to the restriction of the height of the chamber.

According to ISO 3744, the pressure determined sound power can be obtained by:

$$L_W = \bar{L}_p + 10 \lg(S/S_0) \quad (4)$$

in which  $S = 2\pi r^2$  is the area of hemispherical surface,  $S_0 = 1 \text{ m}^2$ , and  $\bar{L}_p$  is the surface time-averaged sound pressure level which can be obtained by correcting the mean time-averaged sound pressure level  $\bar{L}_{p(ST)}$  from background noise,

$$\bar{L}_p = \bar{L}_{p(ST)} - K_1 \quad (5)$$

where  $K_1$  is the background noise correction. Assuming that the microphone positions are allocated with equal segment of areas, the mean time-averaged sound pressure level from arrays of microphones can be calculated as

$$\bar{L}_{p(ST)} = 10 \lg 10 \left( 1/N \sum_{i=1}^N 10^{0.1 L_{pi(ST)}} \right) \quad (6)$$

where  $L_{pi(ST)}$  is the time-averaged sound pressure level at  $i$ th microphone position, and  $N$  the number of microphone positions which is 20 in the present case.

## 5. Results and analyses

The eigen-frequencies of the first 120 modes and their corresponding mode shapes were first identified. Structural mobility and radiated sound power of the test sample subjected to a point

harmonic force were then measured, for plates with/without damping materials. These results are compared against the numerically predicted ones. Additionally, reductions on structural vibration and sound power level were also observed, as detailed later.

### 5.1. Eigen-frequencies and mode shapes

Modal analyses of the manufactured ABH plate were first carried out experimentally. Eigen-frequencies were identified based on the positions of resonant peaks observed from the frequency response curves measured by the laser-vibrometer. The obtained eigen-frequencies of the first 120 modes are presented and compared with their numerically predicted counterparts from the DW model in Fig. 6, showing a good agreement with each other. To quantify the agreement level, the relative error, defined as  $(f_{model} - f_{test})/f_{test} \times 100\%$ , is present in Fig. 7, where  $f_{test}$  and  $f_{model}$  represent the eigen-frequencies obtained from the experimental tests and the DW model, respectively. It can be seen that experimental values are slightly smaller than the predicted ones due to shearing effect of the plate which is neglected in the DW model. Nevertheless, most of the errors are below 2% with the maximum one being 3.74%, which is deemed acceptable.

Further comparisons are performed in terms of mode shapes. Four arbitrarily chosen mode shapes (30th, 50th, 83rd, 119th modes) are presented in Figs. 8–11. To ensure a detailed comparison, different views (front view, side view, and vertical view) of these mode shapes are shown. To capture the local details inside the ABH indentation, 75,000 and 33,233 points are respectively used to depict the mode shapes, obtained from numerical simulations and experiments. It is remarkable to see that experimentally measured mode shapes are in nearly perfect agreement with their numerically predicted counterparts, from low-order to high-order modes. Though signal to noise ratio is a bit low for high-order modes, details in deformation inside the ABH indentation are clearly observable.

As previously mentioned, energy focalization is one of the unique features of the ABH. This can be clearly observed from the measured vibration patterns of the high-order modes, as shown in Figs. 10 and 11. The vibration amplitude inside the ABH indentation is obviously larger than that of the uniform part of the plate, more evident around the ABH center. Meanwhile, the highly compressed waves inside the indentation area can also be clearly observed.

### 5.2. Cross point mobility

Forced vibration analyses were carried out on the test sample with a harmonic excitation applied at (0.518, 0.165) m over the uniform portion. The amplitude of vibration displacement of a number of measured points over the surface of the test sample was measured from 5 Hz to 6000 Hz with an increment of 5 Hz.

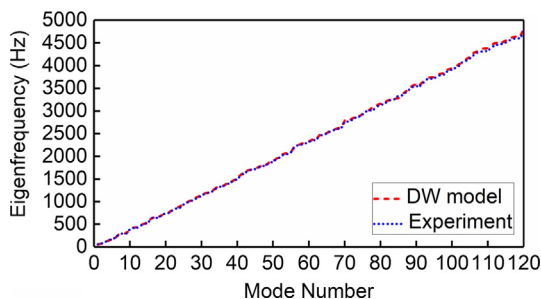


Fig. 6. Eigen-frequencies of the first 120 modes: DW model (short dash line); experiment (short dot line).

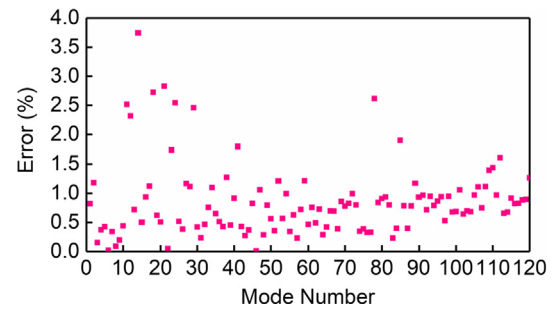


Fig. 7. Relative errors of eigen-frequencies of the first 120 modes obtained from the DW model and experiments.

Mobilities ( $20\lg(v/F)$ ) at three representative points on the test sample were extracted after 10 times averages. These three points include the ABH center (0.3, 0.25) m, a point (0.0375, 0.25) m on the uniform portion and the driving point (0.518, 0.165) m.

Fig. 12(a)–(c) illustrate the comparisons between the experimental results and numerical simulations, which shows a good consistency in nearly the entire frequency range, especially below 5500 Hz. Above 5500 Hz, differences begin to show; this presumably can be attributed to the deviation of the manufactured ABH indentation from the predesigned profile, since the response at high frequencies is supposed to be more sensitive to local details. Nevertheless, it can be seen that the rich dynamics of the system, manifested by a large number of resonant peaks, can be truthfully reproduced by the DW simulation model, testifying the accuracy of the model on one hand, and the accuracy in manufacturing the test sample on the other hand.

The deployment of damping layers inside the ABH indentation plays a crucial role in the realization of ABH effect. To illustrate this effect, the vibration response of the ABH test sample with its central ABH portion covered with 3M™ VHB™ adhesive transfer tape F9473PC was experimentally measured. The density  $\rho_d$ , elastic modulus  $E_d$  and loss factor  $\eta_d$  of this material were evaluated at 4000 Hz [26] and tabulated in Table 2. In the present case, the central area of ABH indentation within a radius of  $R_d = 60$  mm was covered with transfer tape F9473PC of a constant thickness  $h_d = 0.75$  mm. Fig. 13 shows the measured and predicted structural mobilities at (0.0375, 0.25) m, showing again a nice fit with each other. Compared with Fig. 12(b), the overall mobility level of the damped plate shows a general decreasing trend with frequencies alongside a general reduction in the peak levels, which can be attributed to the ABH-induced enhancement in the overall system damping.

### 5.3. Radiated sound power

Following the procedure described in Section 4.2, the sound power radiated from the baffled ABH test sample was measured. Using the same excitation as in the vibration test, the sound power radiated from test sample with/without damping materials was measured. For the sake of comparison, again, the measured sound pressure at each microphone position was normalized by the input force. Subsequently, substitution of averaged sound pressure level into Eq. yields the total sound power as shown in Fig. 14. Comparing the experimentally obtained sound power with that of model simulations, an agreement can be noticed between these two sets of results, both with (Fig. 14(a)) and without (Fig. 14(b)) damping layers.

The results also show that the signal to noise ratio is variable in the frequency range of interest. Due to the low signal to noise ratio in the frequency range between 1000 Hz and 1500 Hz, the

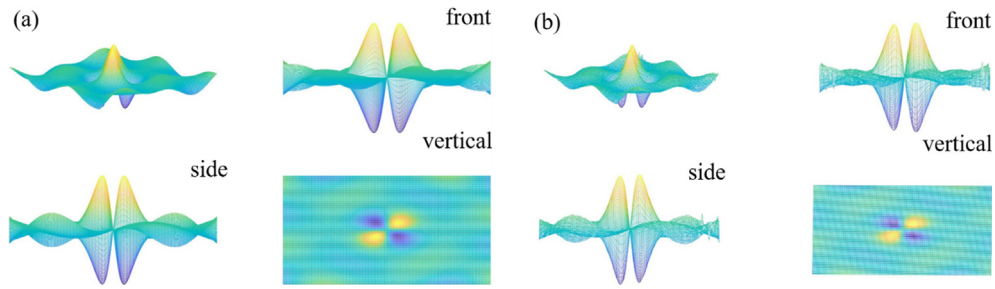


**Fig. 8.** Comparison of 30th mode shape: (a) DW model (left),  $f_n = 1025.8$  Hz; (b) experiment (right),  $f_n = 1014.0$  Hz.

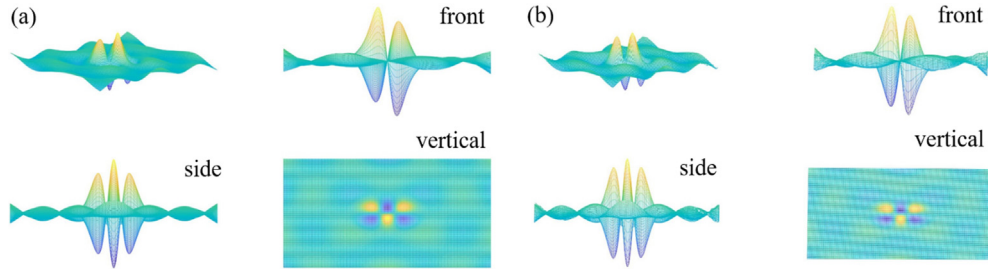


**Fig. 9.** Comparison of 50th mode shape: (a) DW model (left),  $f_n = 1801.4$  Hz; (b) experiment (right),  $f_n = 1782.5$  Hz.

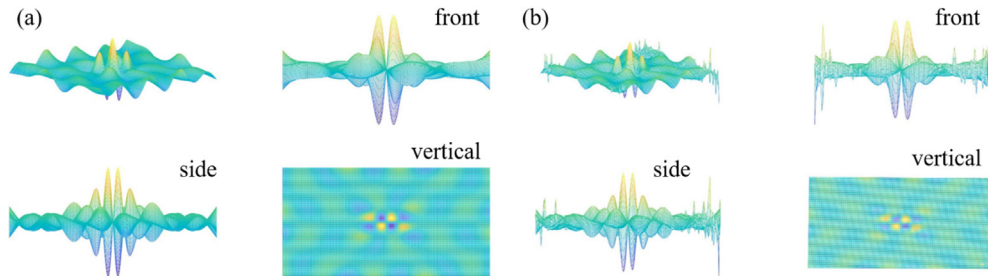


**Fig. 10.** Comparison of 83rd mode shape: (a) DW model (left),  $f_n = 3163.5$  Hz; (b) experiment (right),  $f_n = 3135.0$  Hz.

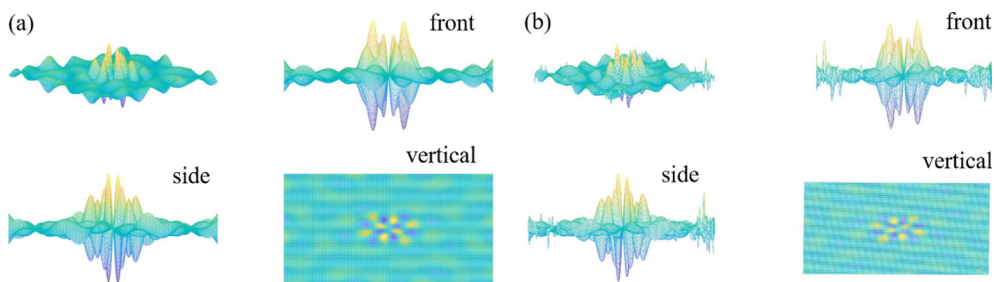


**Fig. 11.** Comparison of 119th mode shape: (a) DW model (left),  $f_n = 4593.7$  Hz; (b) experiment (right),  $f_n = 4556.3$  Hz.

observed sound power is larger than its numerical counterparts. Whereas for other frequency ranges, both sets of results match well. Interference from the shaker should be responsible for the discrepancy between 1000 Hz and 1500 Hz, as the noise from the shaker itself was detected and was difficult to be completely eliminated. Nevertheless, the overall agreement between the model and experiments is deemed satisfactory, especially for such a highly dynamic system exhibiting complex dynamic behaviors.

#### 5.4. Effect of damping layers on ABH performance

As aforementioned, damping layers coated around ABH center are indispensable for the realization of ABH effects and are benefi-

cial to energy dissipation and vibration attenuation. This has been confirmed through experimental tests using the previous test sample. Note the mass of the damping material only accounts for 0.66% of the entire plate. Cross mobility at point (0.0375, 0.25) m over the uniform portion was measured. It can be seen from Figs. 15 and 16 that damping material enables significantly damped vibration peaks as compared with the bare ABH plate, more obvious at high frequencies. Analogously, reduction in the sound power is also observed, especially above the critical frequency of 1995 Hz, estimated using the thickness of the uniform portion of the plate. Therefore, the utilization of realistic damping material deposited at the central portion of the ABH test sample allows for a substantial attenuation of structural vibration response and its radiated

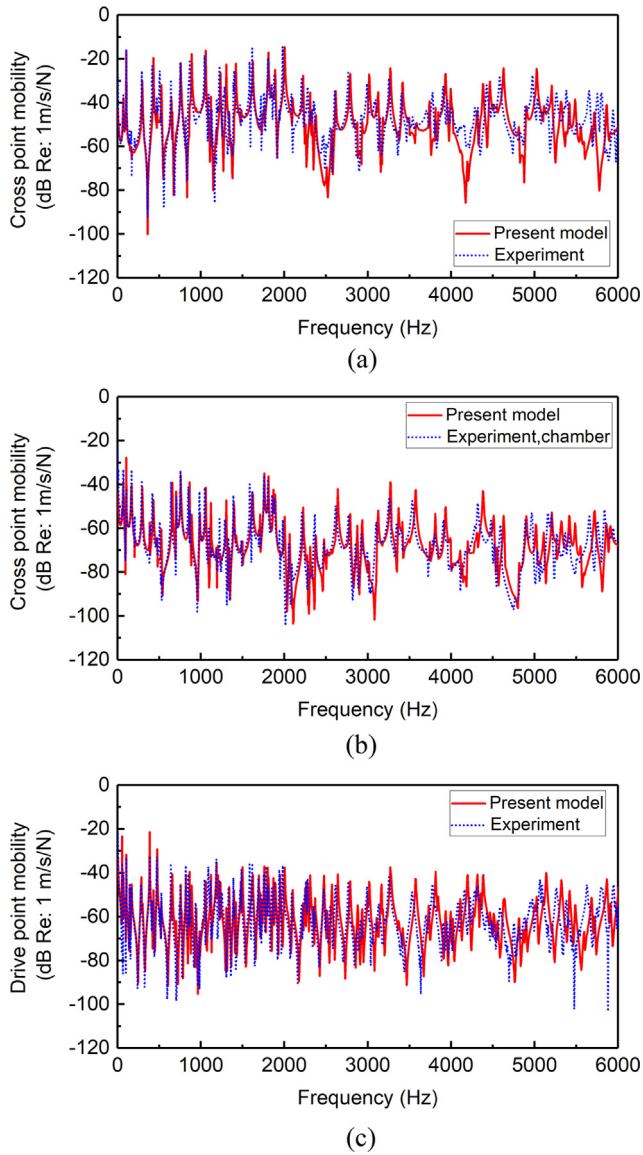


Fig. 12. Cross point mobility of the ABH plate: (a) ABH center (0.3,0.25) m; (b) an arbitrary point (0.0375, 0.25) m on the uniform portion; (c) drive point at (0.518, 0.165) m.

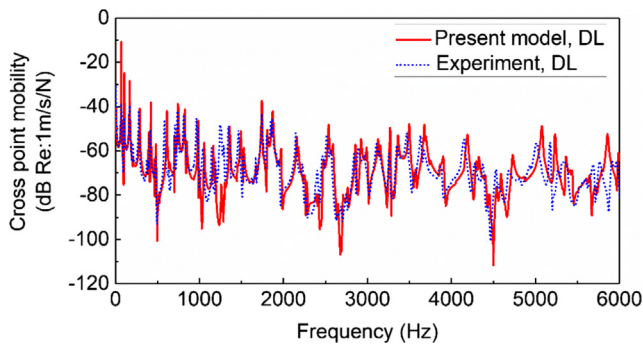


Fig. 13. Comparison of cross point mobility at (0.0375, 0.25) m with damping layers: (a) present model (solid line); (b) experiment (dot line). DL denotes damping layer.

sound power, showing the great potential of ABH structures for vibration and noise control applications. Note that in all test cases, due to the free boundaries of the plates, their sound radiation

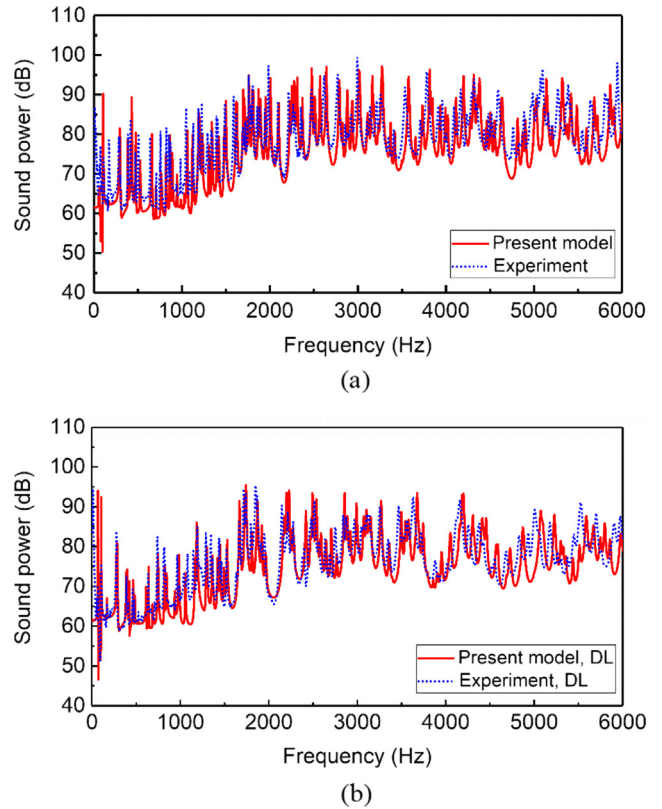


Fig. 14. Radiated sound power: (a) without damping layer; (b) with damping material F9473PC. DL denotes damping layer.

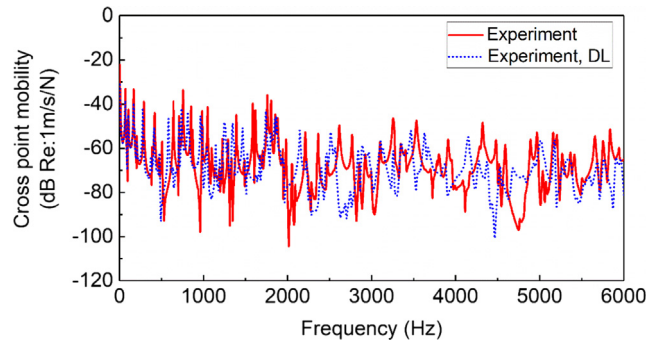


Fig. 15. Measured cross point mobility at (0.0375, 0.25) m on the uniform portion of the test samples: (a) without damping material (solid line); (b) with damping material F9473PC (dot line). DL denotes damping layer.

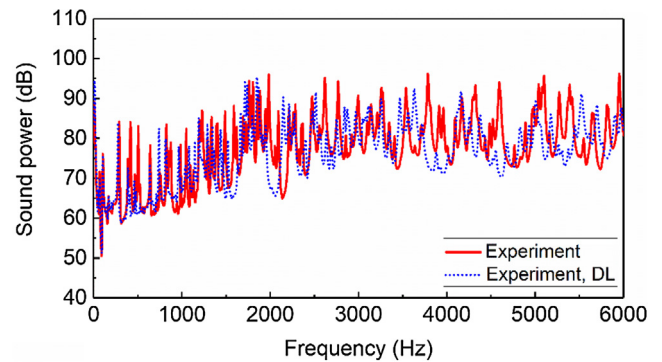


Fig. 16. Measured radiated sound power of test samples: (a) without damping material (solid line); (b) with damping material F9473PC (dot line). DL denotes damping layer.

efficiency at low frequencies are rather low, thus making them less efficient in radiating sound despite their high vibration level in the low frequency range.

## 6. Conclusions

This paper reports a systematic experimental investigation on a rectangular plate embodied with a symmetric circular ABH indentation. Upon a meticulous design and realization of the manufacturing process, a high-precision ABH plate is manufactured and calibrated. Using the manufactured sample, its structural properties, in terms of eigen-frequencies, mode shapes, forced vibration response and radiated sound power, are experimentally tested and compared with a previously developed semi-analytical model. Meanwhile, with realistic damping materials deposited at the central portion of the ABH indentation, ABH effects on reductions in vibration response and sound power are experimentally verified.

The complete set of experimental results, in both vibration and sound radiation perspectives, offer useful benchmark solutions for future ABH studies. As an illustrative example, experimental data have been used to validate a previously proposed DW model. It has been shown that the model provides remarkable accuracy in characterizing the vibration response and sound radiation of the ABH plate which exhibits rich dynamics and complex dynamic behaviors. More specifically, most of the relative errors on the eigen-frequencies of the first 120 modes of the plate are below 2%, alongside a good match in the corresponding mode shapes. Cross point mobilities and the radiated sound power predicted by the DW model also show a good agreement with experimental measurement up to a high frequency range, both with and without deposition of damping materials. Meanwhile, typical ABH phenomena such as wave compression, energy focalization and the effects of viscoelastic damping layers are also clearly observed in experiments, also in agreement with numerical predictions.

It is pertinent to stress that an important outcome of this work is the establishment of a feasible manufacturing procedure of an ABH plate, as well as a full set of well-controlled experimental benchmark solutions on some important vibrational and acoustic metrics. Considering the lack of experimental data and the obvious deficiency in correlating simulations with experiments in the literature, we believe this work would serve as an invaluable data source for future ABH studies.

## Author statement

Authors certify that they have participated sufficiently in the work to take public responsibility for the content, including participation in the experiments, numerical analysis, writing, or revision of the manuscript. Furthermore, each author certifies that this material or similar material has not been and will not be submitted to or published in any other publication if accepted.

## Declaration of Competing Interest

The authors declare that they have no known competing financial interests or personal relationships that could have appeared to influence the work reported in this paper.

## Acknowledgements

Authors thank the Research Grant Council of the Hong Kong SAR (PolyU 152009/17E) and National Science Foundation of China (No. 11532006) for their support.

## References

- [1] Mead DJ, Meador D. *Passive vibration control*. Wiley Chichester; 1998.
- [2] Vemula C, Norris AN. Attenuation of waves in plates and bars using a graded impedance interface at edges. *J Sound Vib* 1996;196:107–27.
- [3] Mironov MA. Propagation of a flexural wave in a plate whose thickness decreases smoothly to zero in a finite interval. *Sov Phys Acoust* 1988;34:318–9.
- [4] Krylov VV. New type of vibration dampers utilising the effect of acoustic 'black holes'. *Acta Acust united Ac* 2004;90:830–7.
- [5] Georgiev VB, Cuenca J, Gautier F, Simon L, Krylov VV. Damping of structural vibrations in beams and elliptical plates using the acoustic black hole effect. *J Sound Vib* 2011;330:2497–508.
- [6] Bowyer EP, Krylov VV. Slots of power-law profile as acoustic black holes for flexural waves in metallic and composite plates. *Structures* 2016;6:48–58.
- [7] Bowyer EP, Krylov VV. Experimental investigation of damping flexural vibrations in glass fibre composite plates containing one-and two-dimensional acoustic black holes. *Compos Struct* 2014;107:406–15.
- [8] Bowyer EP, Krylov VV. Damping of flexural vibrations in turbofan blades using the acoustic black hole effect. *Appl Acoust* 2014;76:359–65.
- [9] Bowyer EP, Krylov VV. Experimental study of sound radiation by plates containing circular indentations of power-law profile. *Appl Acoust* 2015;88:30–7.
- [10] Conlon SC, Fahnline JB, Semperlotti F. Numerical analysis of the vibroacoustic properties of plates with embedded grids of acoustic black holes. *J Acoust Soc Am* 2015;137:447–57.
- [11] Feurtado PA, Conlon SC. An experimental investigation of acoustic black hole dynamics at low, mid, and high frequencies. *J Vib Acoust* 2016;138:061002.
- [12] Krylov VV, Tilman FJBS. Acoustic 'black holes' for flexural waves as effective vibration dampers. *J Sound Vib* 2004;274:605–19.
- [13] Ma L, Cheng L. Sound radiation and transonic boundaries of a plate with an acoustic black hole. *J Acoust Soc Am* 2019;145:164–72.
- [14] Ma L, Zhang S, Cheng L. A 2D Daubechies wavelet model on the vibration of rectangular plates containing strip indentations with a parabolic thickness profile. *J Sound Vib* 2018;429:130–46.
- [15] Zhou T, Tang L, Ji H, Qiu J, Cheng L. Dynamic and static properties of double-layered compound acoustic black hole structures. *Int J Appl Mech* 2017;9:1750074.
- [16] Bayod JJ. Application of elastic wedge for vibration damping of turbine blade. *J Syst Des Dyn* 2011;5:1167–75.
- [17] Zhao L, Semperlotti F. Embedded acoustic black holes for semi-passive broadband vibration attenuation in thin-walled structures. *J Sound Vib* 2017;388:42–52.
- [18] O'Boy DJ, Krylov VV, Kralovic V. Damping of flexural vibrations in rectangular plates using the acoustic black hole effect. *J Sound Vib* 2010;329:4672–88.
- [19] Bowyer EP, O'Boy DJ, Krylov VV, Gautier F. Experimental investigation of damping flexural vibrations in plates containing tapered indentations of power-law profile. *Appl Acoust* 2013;74:553–60.
- [20] Ji H, Luo J, Qiu J, Cheng L. Investigations on flexural wave propagation and attenuation in a modified one-dimensional acoustic black hole using a laser excitation technique. *Mech Syst Signal Proc* 2018;104:19–35.
- [21] Tang L, Cheng L, Ji H, Qiu J. Characterization of acoustic black hole effect using a one-dimensional fully-coupled and wavelet-decomposed semi-analytical model. *J Sound Vib* 2016;374:172–84.
- [22] Tang L, Cheng L. Periodic plates with tunneled Acoustic-Black-Holes for directional band gap generation. *Mech Syst Signal Proc* 2019;133:106257.
- [23] Zhou T, Cheng L. A resonant beam damper tailored with Acoustic Black Hole features for broadband vibration reduction. *J Sound Vib* 2018;430:174–84.
- [24] Bowyer EP, O'Boy DJ, Krylov VV, Horner JL. Effect of geometrical and material imperfections on damping flexural vibrations in plates with attached wedges of power law profile. *Appl Acoust* 2012;73:514–23.
- [25] I. O. f. Standardization, ISO 3744: Acoustics-Determination of sound power levels of noise sources using sound pressure – engineering method in an essentially free field over a reflecting plane, Brussels; 2009.
- [26] Liu W, Ewing MS. Experimental and analytical estimation of loss factors by the power input method. *AIAA J* 2007;45:477–84.